nature COMMUNICATIONS

ARTICLE

DOI: 10.1038/s41467-017-00371-4 OPEN

In situ atomic-scale imaging of the metal/oxide interfacial transformation

Lianfeng Zou[1], Jonathan Li[2], Dmitri Zakharov[3], Eric A. Stach[3] & Guangwen Zhou[1]

Directly probing structure dynamics at metal/oxide interfaces has been a major challenge due to their buried nature. Using environmental transmission electron microscopy, here we report observations of the in-place formation of Cu_2O/Cu interfaces via the oxidation of Cu, and subsequently probe the atomic mechanisms by which interfacial transformation and grain rotation occur at the interfaces during reduction in an H_2 gas environment. The $Cu_2O \rightarrow Cu$ transformation is observed to occur initially along the Cu_2O/Cu interface in a layer-by-layer manner. The accumulation of oxygen vacancies at the Cu_2O/Cu interface drives the collapse of the Cu_2O lattice near the interface region, which results in a tilted Cu_2O/Cu interface with concomitant Cu_2O island rotation. These results provide unprecedented microscopic detail regarding the redox reactions of supported oxides, which differs fundamentally from the reduction of bulk or isolated oxides that requires the formation of new interfaces between the parent oxide and the reduced phase.

[1] Department of Mechanical Engineering & Materials Science and Engineering Program, State University of New York at Binghamton, Binghamton, NY 13902, USA. [2] Department of Physics, Applied Physics and Astronomy & Materials Science and Engineering Program, State University of New York, Binghamton, NY 13902, USA. [3] Center for Functional Nanomaterials, Brookhaven National Laboratory, Upton, NY 11973, USA. Correspondence and requests for materials should be addressed to G.Z. (email: gzhou@binghamton.edu)

Many reactions such as oxidation and reduction, heteroepitaxial growth, and heterogeneous catalysis involve the formation of metal/oxide interfaces, and the resulting interfaces are a critical region in controlling both reaction mechanisms and macroscopic properties. For instance, metal/oxide interfaces act as active sites that enhance catalytic reactivity due to synergy between the support and supported phases[1–4]. Metal/oxide interfaces also serve as a reservoir for oxygen during oxidation, and thus significantly alter the oxidation kinetics[5]. Finally, the nature of the heteroepitaxial alignment between metal nuclei and the metal oxide substrate controls the morphology of the epilayer during thin-film growth[6–8]. Understanding the processes that occur at the metal/oxide interface is crucial for a full mechanistic understanding of many processes and phenomena, as this is where new metal/oxide interactions originate, and thus for further advancing applications that rely on the atomic-level control of the metal/oxide interface.

Unfortunately, probing interfacial dynamics in situ has always been a major challenge, mainly because of the experimental inaccessibility of buried interfaces. Generally, transmission electron microscopy (TEM) offers the opportunity to study static interfaces, but this usually requires complex sample preparation and suffers from the possibility of introducing artifacts and contamination to the interface region. In relation to technologically relevant process such as oxidation/reduction, catalysis, and thin-film growth, metal/oxide interfaces are in fact highly dynamic in their response to and interaction with the environment. Fundamental understanding of interface dynamics not only requires resolving the local structure at the atomic scale, but also the ability to capture this structural evolution in real time and under reaction conditions. TEM has evolved dramatically in recent years and allows for temperature-, time-, and pressure-resolved imaging of gas-surface reactions by introducing a reactive gas to the sample while simultaneously monitoring the structural evolution at the atomic scale[9–16].

Cu-based materials are widely used in different oxidizing/reducing environments for a wide variety of applications, including Cu interconnect technology and heterogeneous catalysis. With all these applications, the exposure of Cu to oxygen results in the generation of a Cu oxide and thus a metal/oxide interface. Switching to hydrogen gas leads to the reduction of the metal oxide. These redox conditions are typical of a number of catalytic gas--surface reactions, such as the water-gas-shift reaction[17], CO oxidation[18], and methanol oxidation[19] as well as catalyst regeneration treatment[20] for which H_2 (or CO) is involved either as a reactant or a reaction product.

In this work, we employ environmental TEM to observe the structural evolution of Cu_2O/Cu interfaces at the atomic scale and in real time in a reducing environment inside the microscope. We have chosen to study the Cu_2O/Cu interface as a model system, in order to probe both interface stability and the phase transformations that occur in the reducing environment. We show that the H_2-induced Cu_2O reduction results in the transformation of $Cu_2O \rightarrow Cu$ via step-flow at the epitaxial Cu_2O/Cu interface. While the epitaxial metal/oxide interface is maintained initially, we find that the transition from an epitaxial to nonepitaxial interface occurs via grain rotation driven by the accumulation of oxygen vacancies at the interface region.

Results

In situ creation of Cu_2O/Cu interfaces. The first step of the study is to create Cu_2O/Cu interfaces, which is achieved through oxidizing a single-crystal Cu(100) thin film (nominal thickness of ~50 nm, see Methods section) inside the TEM. The Cu thin film is first heated at 600 °C in flowing H_2 gas ($pH_2 = 10^{-3}$ Torr) to generate holes with well-defined and atomically clean {100} and {110} facets, as shown in Fig. 1a. The annealed sample is then oxidized at 350 °C to form Cu_2O/Cu interfaces by introducing oxygen gas at $pO_2 = 5\times10^{-3}$ Torr. Figure 1b shows a typical HRTEM image of a Cu_2O/Cu interface generated by the oxidation of a Cu-faceted edge. In situ TEM observations of the Cu_2O/Cu interface dynamics are made in the cross-sectional view.

Oxidation of Cu can produce various phases of Cu oxides, including Cu_2O, Cu_4O_3, and CuO[21]. Thus, identification of the oxide phase that has formed is necessary before investigating the subsequent interfacial reactions that occur during reduction. Measurements of the periodicity and spacing of atomic columns in both the Cu substrate and oxide regions, along with the diffractogram of the whole area, show that the Cu_2O phase is formed, with the epitaxial relation of $Cu_2O(200)//Cu(200)$ and $Cu_2O[001]//Cu[001]$ (Supplementary Note 1). The HRTEM analyses above confirm that an epitaxial Cu_2O layer is formed along the Cu (100) facet.

$Cu_2O \rightarrow Cu$ interfacial transformation. The Cu_2O/Cu interfaces formed from the in situ oxidation are ideally suited for studying interfacial dynamics in a reducing environment. The Cu_2O film is reduced at 350 °C by flowing H_2 gas ($pH_2 = 4\times10^{-2}$ Torr). Figures 2a–c show time-sequence HRTEM images of the Cu_2O/Cu interface during the Cu_2O reduction with the H_2 flow

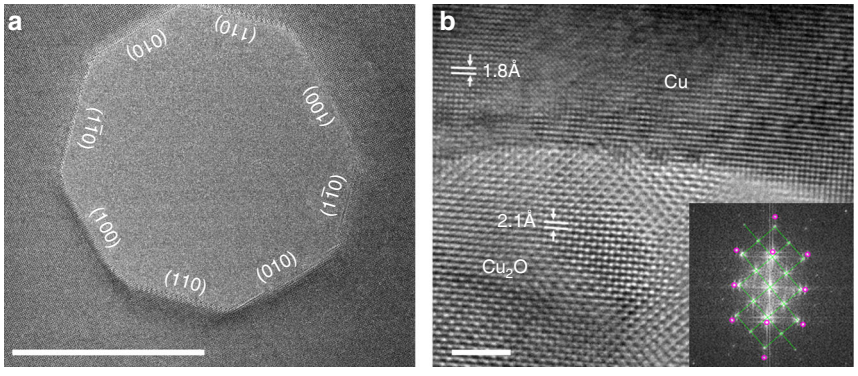

Fig. 1 In situ formation of Cu_2O/Cu interfaces. **a** TEM image of an as-prepared nano-hole in the Cu(100) thin film after annealing at 600 °C in the flow of H_2 gas at $pH_2 = 10^{-3}$ Torr. **b** HRTEM image of a Cu_2O/Cu interface formed by oxidizing a faceted Cu edge to form a Cu_2O layer at 350 °C and $pO_2 = 5\times10^{-3}$ Torr for 5 min. The *inset* to the bottom-right corner is a diffractogram of **b**, where the *green lines* and *purple rings* illustrate the diffraction spots for Cu_2O and Cu phases, respectively. *Scale bar*, 20 nm **a**, 2 nm **b**

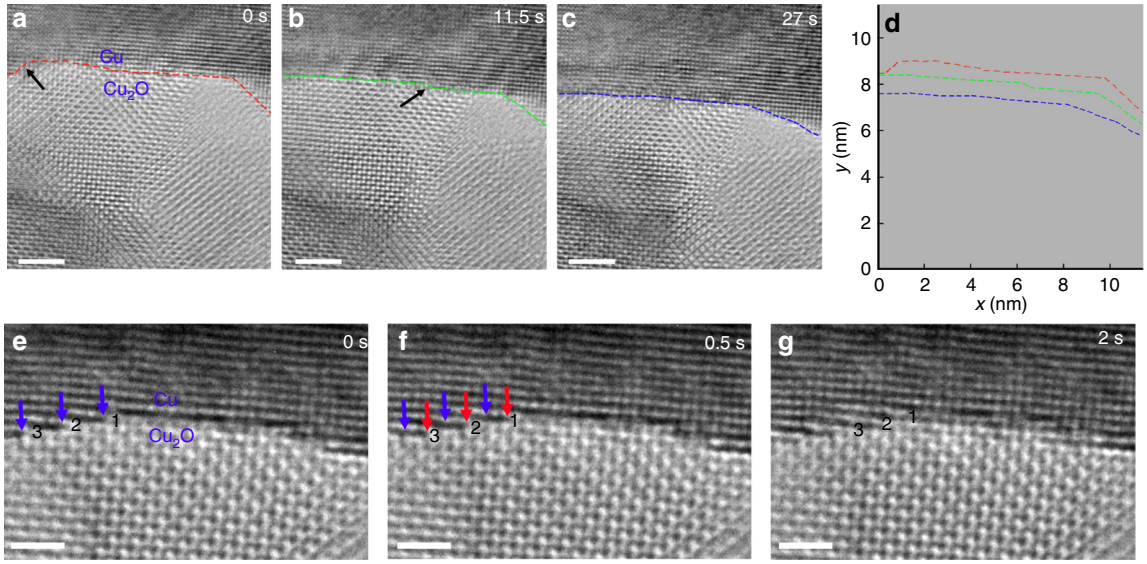

Fig. 2 $Cu_2O \rightarrow Cu$ interfacial transformation. **a**–**c** HRTEM snapshots (Supplementary Movie 1) showing the $Cu_2O \rightarrow Cu$ conversion at the Cu_2O/Cu interface at $T = 350$ °C and $pH_2 = 4 \times 10^{-2}$ Torr, the *colored dash lines* outline the Cu_2O/Cu interface, the *black arrows* mark the interface steps. **d** Traces of the position of the Cu_2O/Cu interface at the different times show that the interface moves toward the Cu_2O layer. **e**–**g** High magnification view of the dynamics of the $Cu_2O \rightarrow Cu$ interfacial conversion at $T = 350$ °C and $pH_2 = 4 \times 10^{-2}$ Torr (Supplementary Movie 2), the *blue* and *red arrows* point to the Cu_2O/Cu interface step edge at 0 s and 0.5 s, respectively. Numbers 1, 2 and 3 mark the horizontal atomic planes at the Cu_2O/Cu interface. *Scale bar*, 2 nm (**a**–**c**), 1 nm (**e**–**g**)

(all the in situ TEM images are aligned to compensate for thermal drift). The red, green and blue dashed lines in Figs. 2a–c outline the location of the Cu_2O/Cu interface. Detailed tracing of the movement of the Cu_2O/Cu interface is depicted in Fig. 2d, where the relative positions of the interface at different times are shown for comparison. The Cu_2O/Cu interface is initially observed to exhibit a wide and flat shape, with the presence of atomic steps at the two corner areas (Fig. 2a). As the reaction progresses, the Cu_2O/Cu interface is observed to migrate toward the Cu_2O side as the Cu_2O is converted into metallic Cu along the Cu_2O/Cu interface (Figs. 2b, c). The Cu_2O/Cu interface maintains the wide and flat morphology and displays an overall normal movement toward the oxide. The interface is measured to migrate by the amount of $\sim 8d_{Cu(200)}$ (~1.4 nm) toward the Cu_2O layer during a time elapse of 27 s (Supplementary Movie 1). Meanwhile, the atomic steps at the Cu_2O/Cu interface tend to smooth out quickly, thereby maintaining the sharply defined and microscopically flat interface during the course of the $Cu_2O \rightarrow Cu$ conversion, i.e., the three atomic layer steps on the left corner of the interface (Fig. 2a) and a single atomic step in the middle of the interface (Fig. 2b), as indicated by the black arrows, are seen to disappear quickly.

Figures 2e–g show snapshots of the $Cu_2O \rightarrow Cu$ interface transformation at a higher magnification view. It can be seen that the $Cu_2O \rightarrow Cu$ conversion starts from the atomic steps at the corner region and propagates laterally via step-flow along the Cu_2O/Cu interface. Figure 2e shows three atomic steps of Cu residing at the Cu_2O/Cu interface, as indicated by the blue arrows. The blue arrows in Fig. 2f point to the same positions as shown in Fig. 2e, the red arrows point to the new locations of the steps after a time interval of 0.5 s. All the three steps are observed to sweep simultaneously and laterally along the in-plane direction (<100>) of the interface. In the subsequent 1.5 s (Fig. 2g), step 1 meets with the Cu step propagating from the right side to form a continuous Cu layer at the interface. Therefore, the $Cu_2O \rightarrow Cu$ interface conversion occurs via the lateral flow of the atomic steps of the Cu substrate, with a coordinated retraction of the Cu_2O at the step edges of the metal and oxide. This interfacial transformation is observed to start at the atomic steps of the Cu_2O/Cu interface, proceed by lateral propagation, and merge with the metallic atomic steps initiated from the other corner area, thereby demonstrating that the step-edge controls the interface reaction. Meanwhile, the epitaxial Cu_2O/Cu interface is maintained because the Cu substrate provides a structure template for the epitaxial growth of new Cu released from the reducing Cu_2O.

Grain rotation at the Cu_2O/Cu interface. Continued reduction of the Cu_2O results in a transition from an epitaxial to a non-epitaxial Cu_2O/Cu interface via the rotation of Cu_2O grains. Figure 3 shows an in situ TEM observation of how oxide reduction induces grain rotation with continued H_2 exposure. Figure 3a marks the starting point (0 s) for this time sequence (the sample has been reduced a while before we move to this area for TEM imaging). The epitaxial relation of the Cu substrate and the Cu_2O grain is $Cu_2O(200)//Cu(200)$ and $Cu_2O[001]//Cu[001]$, as identified from the [001]-zone axis HRTEM images shown in Figs. 3a, b. The $Cu_2O \rightarrow Cu$ transformation that results in the propagation of the Cu_2O/Cu interface into the Cu_2O side while maintaining the epitaxial interface is observed between 0 and 30.5 s, where the interface propagation direction is accurately determined by measuring the change in the lattice spacing (Supplementary Note 3). The dashed lines in Fig. 3b mark the locations of the Cu_2O/Cu interface at $t = 0$ s and $t = 30.5$ s, which clearly show that the Cu lattice grows toward the oxide by consuming the oxide via the interface-controlled process identified in Fig. 2. However, the lattice fringe contrast in the Cu_2O grain shows a sudden change between Figs. 3b, c within just 0.5 s of the time interval. The clearly resolved two-dimensional lattice fringes of the Cu_2O grain seen in Fig. 3b turn into the one-dimensional lattice fringes, as seen in Figs. 3c, d. In contrast, the lattice fringe contrast in the Cu region remains the same over the time, which rules out a possible effect from sample tilting with respect to the incident electron beam during the TEM imaging. Meanwhile, by comparing Figs. 3b, c, it can be

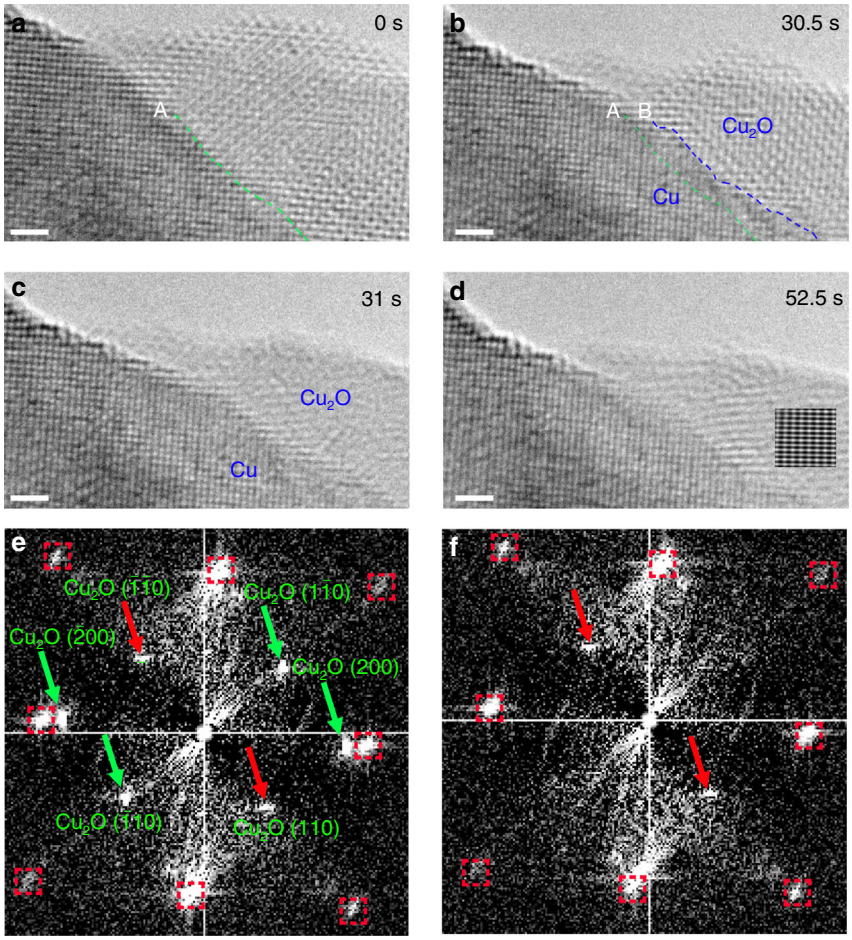

Fig. 3 Cu_2O island rotation along the Cu_2O/Cu interface. **a**–**d** Time-sequence HRTEM images of the $Cu_2O \rightarrow Cu$ reduction at $T = 350$ °C and $pH_2 = 4 \times 10^{-2}$ Torr (Supplementary Movie 3). *Dashed lines* A and B mark the locations of the Cu_2O/Cu interface at 0 s and 30.5 s, respectively. The *inset* in **d** is a simulated HRTEM of the Cu_2O grain tilted by 33° with respect to the <001> direction. **e**, **f** Diffractograms of HRTEM images **b** and **c**, *green* and *red arrows* mark the Cu_2O diffraction spots that disappear and remain, respectively, due to the rotation of the Cu_2O island; the *red dashed squares* mark the Cu diffraction spots, which remain unchanged during the time interval. *Scale bar*, 1 nm

seen that the projected area of the Cu_2O grain becomes smaller within the short time interval. After grain rotation, the Cu_2O grain loses its epitaxy with the Cu substrate: thus it no longer presents a zone-axis orientation with respect to the e-beam. Thus, the Cu_2O/Cu interface transformation cannot be resolved clearly from the TEM imaging (Fig. 3c, d).

We first identify the cause for the sudden change of the lattice fringe contrast in the Cu_2O grain between Figs. 3b, c. Given the apparent loss of the sharp lattice fringe contrast, two possibilities are considered. One possibility is related to a change in the crystal structure of the oxide island: however, this is ruled out by HRTEM image simulation of oxygen deficient Cu_2O structures (Supplementary Note 4). The other possibility is that the entire Cu_2O grain rotates, as induced by the $Cu_2O \rightarrow Cu$ interfacial reduction in such a way that the Cu_2O grain has deviated from the original <001> zone axis orientation. Figure 3e is a diffractogram of the HRTEM image of Fig. 3b, in which the [001]-zone-axis patterns of both Cu and Cu_2O are clearly visible. Fig. 3f is the diffractogram of the HRTEM of Fig. 3c, in which the two {110} spots from the Cu_2O island are still visible (indicate by the red arrows), confirming that the oxide island still remains the Cu_2O structure, while its zone-axis orientation has tilted away from the original <001> direction. The new zone axis for the Cu_2O grain is determined to be $<-a\ a\ 1>$ by the Weiss zone law and the misorientation angle between the Cu substrate and the Cu_2O grain can be quantitatively estimated as 33° from the relation of the projection areas of the Cu_2O grain before and after the rotation (Supplementary Note 5). The simulated diffraction pattern (Supplementary Fig. 6) from the tilted Cu_2O grain has a good match to the diffractogram shown in Fig. 3f, where only diffraction spots from {110} planes are present. We then perform HRTEM image simulation using the Cu_2O model with an incident beam along the <−0.465 0.465 1> direction, which corresponds to the Cu_2O rotation out of the (001) plane by 33° with respect to the <001> zone axis. Inset in Fig. 3d is a simulated HRTEM image along the <−0.465 0.465 1> zone axis of Cu_2O, which shows the one-dimensional lattice fringe contrast, and again has good agreement with the experimental HRTEM image.

Discussion

The reduction of metal oxides has traditionally been described using the nucleation and growth model or the interface model[22–24]. In the nucleation and growth model, the generation of small nuclei of the metallic phase occurs on the parent oxide, the oxide/metal interface advances inward and the reaction interface increases until the growing metal nuclei overlap, as shown schematically in Fig. 4a. In the interface model, the rapid formation of a uniform and continuous layer of the metallic phase on the parent oxide occurs and the reaction boundary moves inward as the reaction proceeds (Fig. 4b). While these

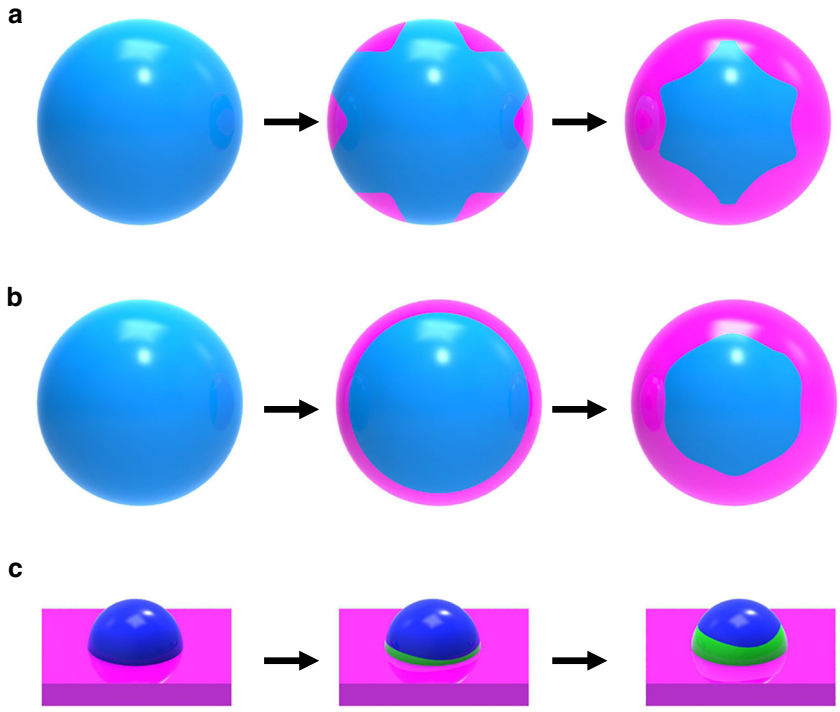

Fig. 4 Schematic comparison of the oxide reduction models. **a** The nucleation and growth model, generation of small nuclei (denoted by *pink color*) of the reduced phase (e.g., a lower valence state oxide or pure metal) occurs on the parent oxide (*blue*) and the reaction interface increases until growing nuclei coalesce and then decreases. **b** The interface model, rapid formation of a uniform layer of a reduced phase (*pink*) on the parent oxide (*blue*) occurs very soon after contacting with a reducing gas. The reaction interface advances inward uniformly as the reaction proceeds, resulting in a spherical core of the oxide that shrinks with time. **c** Reduction of an oxide island (*dark blue*) on a metal support (*pink*), formation of the reduced phase (*green*) occurs preferentially at the buried metal/oxide interface

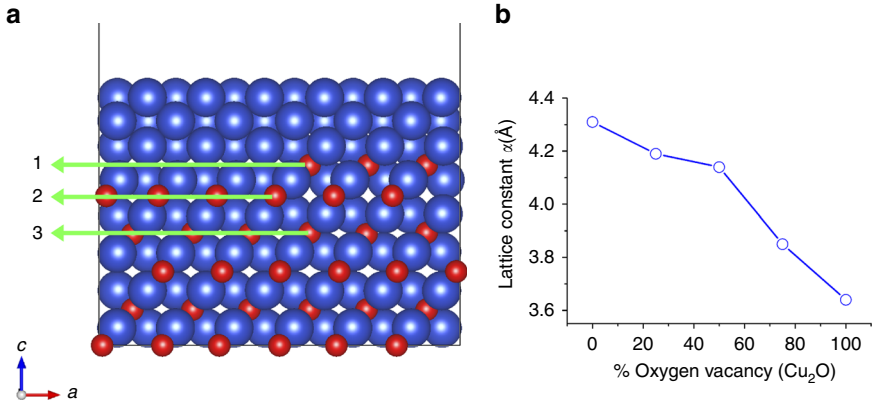

Fig. 5 DFT calculations **a** Oxygen vacancy formation energy (E_{vac}) for three representative interfacial sites, 1: interface step, 2: planar interface, 3: sub-interface. **b** Lattice constant as a function of the concentration of oxygen vacancies in Cu_2O. *Blue* and *red spheres* represent Cu and O atoms, respectively

phenomenological models have been found useful in the description of the reduction of bulk oxides[25, 26], here we find that the reduction of supported Cu_2O islands does not follow either the "nucleation and growth" or "interface" model. Rather than forming metallic Cu on the outer surface of the Cu_2O islands, our in situ TEM observations demonstrate that the reduction of Cu_2O to Cu occurs at the buried Cu_2O/Cu interface (Fig. 4c), where Cu atoms in the parent oxide are directly dislodged to the step edges of the Cu lattice, resulting in step-flow-controlled dynamics. It can be seen that the Cu_2O reduction at the existing Cu_2O/Cu interface still involves the nucleation and growth of Cu at various sites of the Cu_2O/Cu interface, which lead to a rough Cu_2O/Cu interface with the hill-and valley feature (Supplementary Fig. 7). The lateral step-flow along the interface results in the smoothened Cu_2O/Cu interface (as shown in Figs. 2e–g). The thickness of the oxide layer examined in our experiment is typically less 20 nm (i.e., the distance from the Cu_2O/Cu interface to the outer surface of the oxide island). Within this thickness range, we can monitor the structure evolution of the whole Cu_2O grain using in situ HRTEM imaging. However, if the oxide layer is too thick, oxide reduction may also take place at the outer surface of the oxide by following the aforementioned phenomenological "nucleation and growth" model or the "interface" model for the reduction of isolated oxides. The critical thickness of the oxide

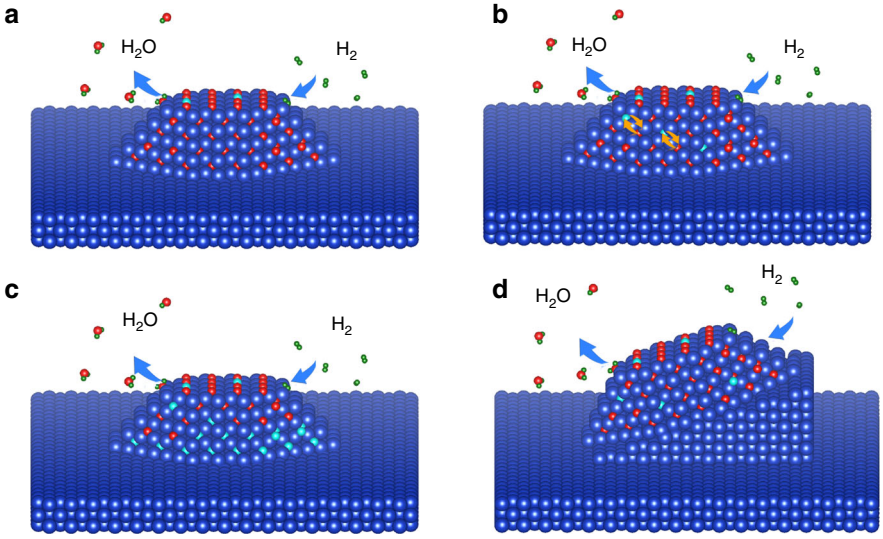

Fig. 6 Pictorial illustration of the Cu_2O island rotation. **a** Reaction of H_2 molecules with lattice oxygen in Cu_2O forms H_2O molecules that desorb from the surface, leaving behind oxygen vacancies. **b** Oxygen vacancies migrate through the oxide layer toward the Cu_2O/Cu interface. **c** Oxygen vacancies accumulate near the Cu_2O/Cu interface region. **d** Abrupt collapse of the Cu_2O lattice in the interface region into Cu results in the formation of a stepped Cu plateau, which drives the rotation of the entire Cu_2O island. *Blue*, *red*, *green* and *cyan spheres* represent Cu, O and H atoms, and O vacancies, respectively

layer that leads to the transition from oxide reduction at the buried metal/oxide interface to the traditional phenomenological models depends on temperature. A higher reaction temperature corresponds to a faster diffusion rate for both H atoms and O vacancies: a thicker oxide layer would be expected in this case. However, thicker oxides are problematic for HRTEM imaging, and thus are beyond our ability to image.

Microscopically, the reduction of metal oxides is a reaction caused by removing lattice oxygen, followed by a subsequent structural rearrangement of the parent lattice. In our case, the reducing species (H_2 molecules) adsorb on the oxide surface and then dissociate into H atoms that may react directly with surface oxygen and/or further penetrate into the oxide and react with lattice oxygen to form hydroxyls. Because of the relatively high temperature (350 °C) employed in our reduction experiments, it is reasonable to expect that hydroxyls exist only as an intermediate and quickly desorb from the surface as H_2O molecules, which leaves behind empty lattice sites (e.g., oxygen vacancies) in the oxide. Evaluation of the reduction activity can be based on the energy needed for removing lattice oxygen, which is defined as vacancy formation energy. Depending on the different sites such as the surface or interface, the oxygen vacancy formation energy can be different, which results in the oxide reduction along the minimum energy path. One would expect the oxide to be stable if oxygen vacancy formation is an energetically costly process. For example, a planar oxide surface usually remains relatively stable when exposed to a low H_2 pressure[24]. In contrast, oxygen atoms may be easily removed at defective sites, i.e., surface steps. To check the stability of lattice O at the metal/oxide interface, we utilized density functional theory (DFT) to investigate energetics of Cu_2O reduction by calculating oxygen vacancy formation energies at three representative sites near the Cu_2O/Cu interface, i.e., an interface step edge, an interface terrace, and a sub-interface layer, as marked by 1, 2, and 3 in Fig. 5a. These are found to be 1.64, 2.1, and 1.98 eV, respectively (Supplementary Note 7). The interface step edge site shows a smaller oxygen vacancy formation energy compared to the planar interface or the sub-interface sites. These DFT results confirm that the oxide reduction along the interface step edge is preferred, consistent with the TEM observation of the step-flow growth of new Cu layers at the Cu_2O/Cu interface during the initial stages of the oxide reduction, as shown in Fig. 2.

While Cu_2O is reduced to Cu at the Cu_2O/Cu interface, oxygen vacancies can be also generated at the oxide surface (Fig. 6a) because it is the first place for H_2 adsorption and dissociation. The oxygen vacancies generated at the surfaces can migrate toward the Cu_2O/Cu interface via exchange with adjacent oxygen atoms (Fig. 6b). When the $Cu_2O \rightarrow Cu$ interfacial conversion does not keep up with the incoming flux of oxygen vacancies, oxygen vacancies then accumulate at the Cu_2O/Cu interface (Fig. 6c). This is also apparent in our in situ TEM observations, which show that no structural changes are detected in the bulk of the oxide while the interface is undergoing the $Cu_2O \rightarrow Cu$ conversion (Figs. 2 and 3). This indicates that the bulk has a much lower oxygen vacancy concentration when compared to the Cu_2O/Cu interface region. This is consistent with our DFT calculation (Fig. 5b), which shows that the lattice parameter of the oxide has a larger tendency to collapse into the Cu lattice when the oxygen vacancy concentration reaches a critical value (e.g., 50%). The abrupt collapse of the oxide lattice will result in the Cu_2O/Cu interface decohesion. The rotation of the Cu_2O grain shown in Figs. 3b, c) is induced by the anisotropic shrinkage of the Cu_2O lattice, as illustrated in Fig. 6d. Cu atoms liberated from the collapse of the Cu_2O lattice near the Cu_2O/Cu interface region aggregate near the corner area, which results in the formation of a stepped Cu plateau at that location. As a result, the initially flat and epitaxial Cu_2O/Cu interface becomes highly tilted, which provides the driving force for the grain rotation that is seen experimentally.

In summary, we use an in situ approach to create Cu_2O/Cu interfaces by oxidation of Cu and subsequently monitor the metal/oxide interfacial transformation induced by the reaction with H_2. Our real time, atomic-scale imaging of the dynamics of how Cu_2O islands transform when subjected to a reducing gas environment demonstrates that the Cu_2O reduction occurs initially via the layer-by-layer retraction of the Cu_2O lattice, with the coordinated growth of the Cu lattice controlled by step-flow along the Cu_2O/Cu interface. Continued accumulation of oxygen vacancies at the Cu_2O/Cu interface region results in the abrupt collapse of the Cu_2O lattice with the concomitant formation of a tilted Cu_2O/Cu interface, which then drives the rotation of the

Cu_2O islands. These results demonstrate that the reduction dynamics of Cu_2O islands are governed by atomic processes occurring at the Cu_2O/Cu interface: an observation which is fundamentally different from the mechanisms known to be associated with the reduction of bulk or isolated oxides. Because the formation of oxide islands is a common phenomenon during the oxidation of metals, and because supported oxides are widely used in heterogeneous catalysis, our results reveal the unique role of the oxide/metal interfaces in controlling the reaction mechanism. These observations have broader implications for understanding and manipulating the way that buried interfaces can affect gas-surface reaction kinetics.

Methods

Sample preparation and in situ TEM characterization. Single-crystal Cu(100) thin films with a normal thickness of 50 nm were grown on NaCl(100) in a ultrahigh vacuum e-beam evaporation system. The as-prepared Cu thin film was then removed from the substrate by dissolving the NaCl in deionized water and mounted on a Si_3N_4 membrane window with 200-nm pores for TEM observation. In situ TEM experiments were performed using a dedicated environmental TEM (FEI Titan 80–300) equipped with an objective-lens aberration corrector. The microscope has a spatial resolution of 0.8 Å in the high-resolution TEM mode, even at the elevated temperature and pressure local to the sample.

In situ TEM imaging of Cu_2O/Cu interfacial transformation. The experiment involves three essential steps for the in situ formation of Cu_2O/Cu interfaces and subsequent observation of the Cu_2O/Cu interfacial transformation. The first step is annealing of a Cu thin film inside the microscope at 600 °C with H_2 gas flowing at a pressure of 10^{-3} Torr for 20 min. This gradually both cleans and thins the sample, resulting in the formation of holes with faceted edges (dominated by (100) and (110) facets). These freshly created facets are atomically clean and ideal for subsequent oxide growth by exposing the sample to oxygen gas. The second step is therefore the creation of the Cu_2O/Cu interface by oxidizing the faceted Cu edges. This is done by pumping the H_2 out of the microscope, and then immediately providing oxygen gas at the pressure of $pO_2 = 5\times10^{-3}$ Torr and $T = 350$ °C for 10 min. In order to observe the subsequent reduction of the newly formed oxide, the oxygen gas is pumped away, and then H_2 gas is again inserted into the chamber. In situ TEM observation of the oxide reduction process is by imaging along the Cu_2O/Cu interface under the flow of H_2 gas at $pH_2 = 4\times10^{-2}$ Torr and 350 °C. To overcome any potential e-beam effects (i.e., to rule them out as factors affecting the in situ TEM results and to ensure that we have studied the intrinsic behavior of the oxide reduction), we employed a first-of-its kind direct electron camera (K2) which allows for fast image acquisition (400 frames per second) with a significantly reduced electron dose rate. We examined the possible effect of electron beam irradiation by comparing the oxide reduction in areas that had been irradiated with electron beam and different sample areas that had not. The in situ TEM images given in Supplementary Note 8 exemplify these "comparison" experiments, which showed that the Cu_2O islands with a thickness of ~10 nm from the Cu_2O/Cu interface to the outer surface can be reduced completely to metallic Cu after 5 min of H_2 gas flow at $pH_2 = 1\times10^{-3}$ Torr and $T = 350$ °C, irrespective of whether the e-beam was irradiating the sample or not. Conducting experiments of this type to understand the effect of electron irradiation is part of our experimental protocol, and in this case ensured that electron irradiation has a negligible effect on the observed oxide reduction process.

DFT calculations. DFT calculations are performed using the Vienna ab-initio simulation package[27–29] with the PW91 generalized gradient approximation[30] and projector augmented wave[31] potentials. Our previous works have confirmed that a cutoff energy of 380 eV is sufficient to give a well converged system energy[32]. The Brillouin-zone integration is performed using $(4\times4\times1)$ K-point meshes based on Monkhorst-Pack grids[33] and with broadening of the Fermi surface according to Methfessel-Paxton smearing technique[34] with a smearing parameter of 0.2 eV. The interface model is simulated by placing the interface between four layers of Cu(100) and four layers of Cu_2O(100) as shown in Fig. 5a. Each Cu layer in Cu and Cu_2O contains eight Cu atoms, and each O layer in Cu_2O contains four O atoms, while the step interface contains two O atoms. The top layer of Cu and the bottom layers of Cu_2O are fixed at the lattice position and all other atoms are allowed to fully relax during optimization until all force components acting on the atoms are below 0.02 eV/Å. Successive slabs are separated by a vacuum region of at least 13 Å.

The oxygen vacancy formation energy E_{vac} is calculated using the following equation

$$E_{vac} = E_{tot} - E_{ref} + \frac{N_0}{2}E_{O_2}, \quad (1)$$

Where, E_{tot} is the total energy of the Cu-O system containing N_o number of oxygen vacancies, E_{ref} is the energy of the structure without the oxygen vacancies, and E_{O_2} is the energy of an isolated oxygen molecule. The atomic structures are visualized using the VESTA package.

There are two different approaches used to study the interface formed by the two phases. The first one, called the (1×1) model, uses one unit cell in the plane of the interface for each phase and is used for phases with a relatively small mismatch. The lattice parameters are scaled until the phases of the interface match perfectly. This is the primary method used in first principles studies of interface models[35–38]. The second approach consists of determining the ratio of two integers that is closest to the ratio of lattice parameters in the interface. This method leads to incoherent or semi-coherent interface models with minimized mismatch[35].

In the case of Cu and Cu_2O phases, the ratio between the lattice parameters of Cu to Cu_2O is ~0.84, Cu and Cu_2O having calculated bulk lattice parameters of 3.64 and 4.31 Å, respectively. Using the second approach, this ratio could be approximated by 5/6, with an interface model $(5\times5)Cu_2O$ /(6×6)Cu. Previous studies have shown that the epitaxial growth of Cu_2O thin films on Cu substrates results in a (5×6) coincidence site lattice at the Cu_2O/Cu interface[6]. This interface model significantly reduced the strain to ~1.48%. However, in performing DFT calculations of the oxide islanding during oxidation, the system size reaches up to 516 total atoms. Such an interface model is too large and computationally expensive for many DFT calculations. Wang et al.[39]compared both approaches in a study of Si/Cu interfaces perpendicular to the [111] direction. Even with a large mismatch of 35% between Si and Cu, they showed that a full relaxation of a (1×1) interface model only overestimates the work of separation of the interface (2×2)Si/(3×3)Cu model by ~3%. Regarding the Cu_2O/Cu interface, a previous study also adopted the (1×1) model for calculations on the Cu_2O/Cu interfaces perpendicular to the [111] direction. Therefore, the (1×1) model can be used as a reasonable approach for the Cu_2O/Cu interface perpendicular to the [100] direction.

Data availability. All data generated or analyzed during this study are included in this published article (and its supplementary information files).

Received: 21 October 2016 Accepted: 23 June 2017
Published online: 21 August 2017

References

1. Hendriksen, B., Bobaru, S. & Frenken, J. Oscillatory CO oxidation on Pd (100) studied with in situ scanning tunneling microscopy. *Surf. Sci* **552**, 229–242 (2004).
2. Lad, R. J. Interactions at metal/oxide and oxide/oxide interfaces studied by ultrathin film growth on single-crystal oxide substrates. *Surf. Rev. Lett* **2**, 109–126 (1995).
3. Cargnello, M. et al. Control of metal nanocrystal size reveals metal-support interface role for ceria catalysts. *Science* **341**, 771–773 (2013).
4. Fu, Q., Saltsburg, H. & Flytzani-Stephanopoulos, M. Active nonmetallic Au and Pt species on ceria-based water-gas shift catalysts. *Science* **301**, 935–938 (2003).
5. Schalow, T. et al. Oxygen storage at the metal/oxide interface of catalyst nanoparticles. *Angew. Chem. Int. Ed.* **44**, 7601–7605 (2005).
6. Zhou, G. Metal-oxide interfaces at the nanoscale. *Appl. Phys. Lett.* **94**, 233115 (2009).
7. Jeurgens, L. P., Wang, Z. & Mittemeijer, E. J. Thermodynamics of reactions and phase transformations at interfaces and surfaces. *Int. J. Mater. Res.* **100**, 1281–1307 (2009).
8. Reichel, F., Jeurgens, L., Richter, G., van Aken, P. & Mittemeijer, E. The origin of high-mismatch orientation relationships for ultra-thin oxide overgrowths. *Acta. Mater.* **55**, 6027–6037 (2007).
9. Tao, F. F. & Crozier, P. A. Atomic-scale observations of catalyst structures under reaction conditions and during catalysis. *Chem. Rev.* **116**, 3487–3539 (2016).
10. Tao, F. F. & Salmeron, M. In situ studies of chemistry and structure of materials in reactive environments. *Science* **331**, 171–174 (2011).
11. Gai, P. L., Sharma, R. & Ross, F. M. Environmental (S) TEM studies of gas–liquid–solid interactions under reaction conditions. *MRS. Bull.* **33**, 107–114 (2008).
12. Sharma, R. Design and applications of environmental cell transmission electron microscope for in situ observations of gas–solid reactions. *Microsc. Microanal.* **7**, 494–506 (2001).
13. Hansen, P. L. et al. Atom-resolved imaging of dynamic shape changes in supported copper nanocrystals. *Science* **295**, 2053–2055 (2002).
14. Ross, F. M. Controlling nanowire structures through real time growth studies. *Rep. Prog. Phys.* **73**, 114501 (2010).
15. LaGrow, A. P., Ward, M. R., Lloyd, D. C., Gai, P. L. & Boyes, E. Visualizing the Cu/Cu_2O interface transition in nanoparticles with environmental STEM. *J. Am. Chem. Soc.* **139**, 179–185 (2017).
16. Wu, Y. A. et al. Visualizing redox dynamics of a single Ag/AgCl heterogeneous nanocatalyst at atomic resolution. *ACS Nano* **10**, 3738–3746 (2016).

17. Li, Y., Fu, Q. & Flytzani-Stephanopoulos, M. Low-temperature water-gas shift reaction over Cu-and Ni-loaded cerium oxide catalysts. *Appl.Catal. B* **27**, 179–191 (2000).
18. Huang, T.-J. & Tsai, D.-H. CO oxidation behavior of copper and copper oxides. *Catal. Lett.* **87**, 173–178 (2003).
19. Behrens, M. et al. The active site of methanol synthesis over $Cu/ZnO/Al_2O_3$ industrial catalysts. *Science* **336**, 893–897 (2012).
20. Argyle, M. D. & Bartholomew, C. H. Heterogeneous catalyst deactivation and regeneration: a review. *Catal* **5**, 145–269 (2015).
21. Li, J., Vizkelethy, G., Revesz, P., Mayer, J. & Tu, K. Oxidation and reduction of copper oxide thin films. *J. Appl. Phys.* **69**, 1020–1029 (1991).
22. Ertl, G., Knozinger, H. & Weitkamp, J. *Handbook of heterogeneous catalysis* (VCH, 1997).
23. Kung, H. H. *Transition metal oxides: surface chemistry and catalysis* (Elsevier, 1989).
24. Scholz, J. & Langell, M. Kinetic analysis of surface reduction in transition metal oxide single crystals. *Surf. Sci.* **164**, 543–557 (1985).
25. Rodriguez, J. A., Hanson, J. C., Frenkel, A. I., Kim, J. Y. & Pérez, M. Experimental and theoretical studies on the reaction of H_2 with NiO: role of O vacancies and mechanism for oxide reduction. *J. Am. Chem. Soc.* **124**, 346–354 (2002).
26. Zhou, G. & Yang, J. C. Reduction of Cu_2O islands grown on a Cu(100) surface through vacuum annealing. *Phys. Rev. Lett.* **93**, 226101 (2004).
27. Kresse, G. & Furthmüller, J. Efficiency of ab-initio total energy calculations for metals and semiconductors using a plane-wave basis set. *Comput. Mater. Sci.* **6**, 15–50 (1996).
28. Kresse, G. & Hafner, J. Ab initio molecular dynamics for liquid metals. *Phys. Rev. B* **47**, 558 (1993).
29. Kresse, G. & Hafner, J. Ab initio molecular-dynamics simulation of the liquid-metal–amorphous-semiconductor transition in germanium. *Phys. Rev. B* **49**, 14251 (1994).
30. Perdew, J. P. et al. Atoms, molecules, solids, and surfaces: Applications of the generalized gradient approximation for exchange and correlation. *Phys. Rev. B* **46**, 6671 (1992).
31. Blöchl, P. E. Projector augmented-wave method. *Phys. Rev. B* **50**, 17953 (1994).
32. Li, L., Liu, Q., Li, J., Saidi, W. A. & Zhou, G. Kinetic barriers of the phase transition in the oxygen chemisorbed Cu(110)-(2 × 1)-O as a function of oxygen coverage. *J. Phys. Chem. C* **118**, 20858–20866 (2014).
33. Monkhorst, H. J. & Pack, J. D. Special points for Brillouin-zone integrations. *Phys. Rev. B* **13**, 5188 (1976).
34. Methfessel, M. & Paxton, A. High-precision sampling for Brillouin-zone integration in metals. *Phys. Rev. B* **40**, 3616 (1989).
35. Dalverny, A.-L., Filhol, J.-S. & Doublet, M.-L. Interface electrochemistry in conversion materials for Li-ion batteries. *J. Mater. Chem.* **21**, 10134–10142 (2011).
36. Hashibon, A. & Elsässer, C. Approaches to atomistic triple-line properties from first-principles. *Scr. Mater* **62**, 939–944 (2010).
37. Hashibon, A., Elsässer, C., Mishin, Y. & Gumbsch, P. First-principles study of thermodynamical and mechanical stabilities of thin copper film on tantalum. *Phys. Rev. B* **76**, 245434 (2007).
38. Martin, L., Vallverdu, G., Martinez, H., Le Cras, F. & Baraille, I. First principles calculations of solid–solid interfaces: an application to conversion materials for lithium-ion batteries. *J. Mater. Chem.* **22**, 22063–22071 (2012).
39. Wang, X.-G. & Smith, J. R. Si/Cu interface structure and adhesion. *Phys. Rev. Lett.* **95**, 156102 (2005).

Acknowledgements

This work was supported by U.S. Department of Energy, Office of Basic Energy Sciences, Division of Materials Sciences and Engineering under Award no. DE-SC0001135. J.L. was supported by National Science Foundation via Awards CBET-1264940 and CMMI-105661 for the computational work. The authors thank Yinkai Lei who developed the code for generating the 3D graphics. Research carried out in part at the Center for Functional Nanomaterials, Brookhaven National Laboratory, which is supported by the U.S. Department of Energy, Office of Basic Energy Sciences, under Contract no. DE-SC0012704. This work used the computational resources from the Extreme Science and Engineering Discovery Environment (XSEDE), which is supported by National Science Foundation grant number OCI-1053575.

Author contributions

G.Z. and L.Z. conceived and designed the experiments. L.Z., D.Z. and E.A.S. performed the experiments. J.L. conducted DFT calculations. L.Z. and G.Z. analyzed data and wrote the paper. All the authors commented on the manuscript.

Additional information

Supplementary Information accompanies this paper at doi:10.1038/s41467-017-00371-4.

Competing interests: The authors declare no competing financial interests.

Reprints and permission information is available online at http://npg.nature.com/reprintsandpermissions/

Publisher's note: Springer Nature remains neutral with regard to jurisdictional claims in published maps and institutional affiliations.

Open Access This article is licensed under a Creative Commons Attribution 4.0 International License, which permits use, sharing, adaptation, distribution and reproduction in any medium or format, as long as you give appropriate credit to the original author(s) and the source, provide a link to the Creative Commons license, and indicate if changes were made. The images or other third party material in this article are included in the article's Creative Commons license, unless indicated otherwise in a credit line to the material. If material is not included in the article's Creative Commons license and your intended use is not permitted by statutory regulation or exceeds the permitted use, you will need to obtain permission directly from the copyright holder. To view a copy of this license, visit http://creativecommons.org/licenses/by/4.0/.

© The Author(s) 2017